



## Research Article

<https://doi.org/10.1631/jzus.A2400345>



# Dynamic response of the ground beneath a high-speed railway based on typical upper Shanghai clays involving water table change

Jing HU<sup>1</sup>✉, Chengming YE<sup>1</sup>, Juntao JIANG<sup>1</sup>, Shujing WU<sup>1</sup>, David THOMPSON<sup>2</sup>, Xuecheng BIAN<sup>3</sup>

<sup>1</sup>College of Civil Engineering, Fuzhou University, Fuzhou 350108, China

<sup>2</sup>Institute of Sound and Vibration Research, University of Southampton, Highfield, Southampton SO17 1BJ, UK

<sup>3</sup>MOE Key Laboratory of Soft Soils and Geoenvironmental Engineering, Department of Civil Engineering, Zhejiang University, Hangzhou 310058, China

**Abstract:** A rising water table increases soil water content, reduces soil strength, and amplifies vibrations under identical train loads, thereby posing greater risks to train operations. To investigate this phenomenon, we used a 2.5D finite element (FE) model of a coupled vehicle–embankment–ground system based on Biot’s theory. The ground properties were derived from a typical soil profile of the Yangtze River basin, using geological data from Shanghai, China. The findings indicate that a rise in the water table leads to increased dynamic displacements of both the track and the ground. This amplification effect extends beyond the depth of the water table, impacting the entire embankment–foundation cross-section, and intensifies with higher train speeds. However, the water table rise has a limited impact on the critical speed of trains and dominant frequency contents. The dynamic response of the embankment is more significantly affected by water table rises within the subgrade than by those within the ground. When the water table rises into the subgrade, significant excess pore pressure is generated inside the embankment, causing a substantial drop in effective stress. As a result, the stress path of the soil elements in the subgrade approaches the Mohr-Coulomb failure line, increasing the likelihood of soil failure.

**Key words:** Dynamic response; Excess pore pressures; Water table rise; High-speed train; 2.5D finite element (FE) model

## 1 Introduction

Compared to traditional railways, high-speed trains (HSTs) induce significant track–ground vibrations, increasing train operational risks. This issue is particularly serious when trains approach critical speeds, causing a resonant-like effect (Madshus and Kaynia, 2000; Costa et al., 2015; Hu et al., 2019). Simultaneously, the frequency of extreme rainstorms has risen globally, increasing groundwater storage in upper soil layers (Huang et al., 2021). For example, Southeast China experienced an increase of  $3.799 \times 10^9 \text{ m}^3$  in groundwater storage within the Yangtze River basin between 2019 and 2020, raising the shallow water table by 0.5 to 2.0 m (Huang et al., 2021). The dynamic behaviour of the track–ground system is closely related to

the soil properties of the embankment and foundation. A rising water table increases soil water content, reduces soil strength (Duong et al., 2013), and amplifies vibrations under the same train load (Jiang et al., 2016a; Hu et al., 2023). Additionally, excess pore pressure in the soil alters stress distribution, thereby posing greater threats to train operations. To mitigate these risks and support the demand for faster trains, studying the dynamic response of high-speed railways in relation to changes in the water table is essential.

Several studies have directly measured the dynamic responses and deformation of railway embankments under different water tables through large-scale model tests. Jiang et al. (2016a) established a full-scale physical model of a ballastless track and studied the dynamic responses of the embankment as the water table rose from the bottom to the surface. They found that the vibration response of the embankment increased significantly due to the rise in groundwater level. Other full-scale physical model investigations by Huang et al. (2019) and Chen et al. (2014) drew similar conclusions.

✉ Jing HU, [jingh@fzu.edu.cn](mailto:jingh@fzu.edu.cn)

Jing HU, <https://orcid.org/0000-0003-0495-2749>

Received July 16, 2024; Revision accepted Nov. 26, 2024;  
Crosschecked July 30, 2025

© Zhejiang University Press 2025

Constructing large-scale model testing equipment is often both challenging and costly. As a result, researchers frequently use analytical and semi-analytical methods to study wave characteristics in saturated foundations under moving loads. Some of the studies on the dynamic response of porous media are summarized in Fig. 1. Notably, most current research relies on linear elastic models. Although natural soil behavior is generally nonlinear, the stress within embankments remains mainly within the elastic strain range due to the strength of artificial fill materials. Furthermore, stress diffusion in the embankment results in a ground foundation stress typically below 10 kPa (Hu and Bian, 2022b). Thus, even in natural soil, stress levels largely stay within the elastic range, making linear elasticity theory a reasonable approach for analyzing the dynamic response of saturated foundations.

For high-speed railways, the track structure's consistent geometry and material properties along the longitudinal direction have led some researchers to apply the 2.5D finite element method (FEM) to analyze dynamic responses (Gao et al., 2012, 2014; Hu and Bian, 2022a). Bian et al. (2019) and Hu et al. (2021) established 2.5D finite element (FE) models of a high-speed railway embankment on a saturated foundation to investigate the effects of the saturated soil permeability coefficient and train speed on the dynamic response. Despite significant advancements in computational efficiency, existing FEMs are still based mainly on constitutive models of single-phase media, and dynamic solutions for saturated media remain limited.

A rise in water table induces a transition in some foundation and embankment soil from an approximate

single-phase state with minimal water content to a saturated state. Consequently, considerations regarding water table rise entail addressing key issues such as multi-layer soil dynamics and the transformation of certain soil layers from a single-phase to a saturated medium. To date, analytical methods have encountered challenges in solving dynamic problems involving multi-layered saturated media. Additionally, existing 2.5D FE models treat the foundation mainly as entirely saturated soil, overlooking variations in the water table within both the foundation and embankment.

To address these deficiencies, we propose the establishment of a 2.5D FE model that combines single-phase and saturated media. The rise of the water table is simulated by transitioning from a single-phase to a saturated medium. Considering that the Yangtze River basin hosts some of the world's largest and busiest HST lines, a representative soil layer from Shanghai, China was used to exemplify the foundation characteristics in this region. Subsequently, the dynamic response of the railway embankment and foundation under HST loads was simulated for a variable water table, ranging from within the foundation to the surface of the embankment. We examined the effects of water table rise on dynamic displacement, excess pore pressure, and effective stress.

## 2 Typical upper Shanghai clays

Shanghai is not only one of the largest and most prosperous cities in the world, but it is also at the heart of the Yangtze River basin in China. Due to numerous

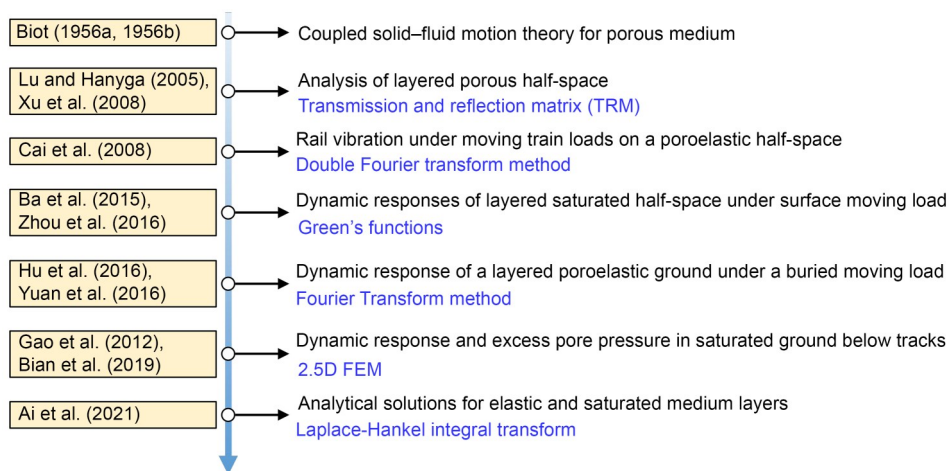


Fig. 1 Brief summary of studies on the dynamic response of porous media

underground projects over the last few decades, the engineering properties of Shanghai upper clays have been extensively studied (Dassargues et al., 1991; Schroeder et al., 1992; Ng et al., 2011). From a geological perspective, the upper Shanghai clay is part of the modern Yangtze River basin, and thus its geological characteristics can be taken as broadly representative of the area. The Quaternary soil layer in Shanghai can be divided into upper and lower parts according to the different sedimentary components of the soil layer. The lower part is early Pleistocene continental sedimentary soil, with a buried depth of generally more than 145 m, and is an interlayer of clay and gray-white sand (Wu, 2016). The upper part, which is relevant to modern engineering construction, is deposited where the marine environment had gradually advanced following frequent infringements since the Middle Pleistocene period. Its buried depth is less than 145 m, and it is an interlayer of clay, light gray, and yellow-gray sand (Yan and Shi, 2006; Wu, 2016). More specifically, in the range down to 70 m below the surface, it consists mainly of loose sediments of marine facies formed by the alternation of sea and land since the Middle Pleistocene (Wu, 2016). In other words, this part of the stratum is interdeposited with soft clay and sand, layer by layer. According to the sedimentation of the modern Yangtze River basin since the Mid-Holocene (Dassargues et al., 1991), upper Shanghai clays can be divided approximately into six layers (Fig. 2) (Bai, 2014; Shen et al., 2014). These can be identified as: (1) crust layer, (2) first sand layer, (3) first compression layer, (4) second sand layer, (5) second compression layer, and (6) first hard soil layer. Based on the above geological conclusions and the division of the engineering geological and hydrogeological districts of upper Quaternary Shanghai

soil layers reported by Dassargues et al. (1991) and Wu (2016), a simplified layering of typical foundation soil for upper Shanghai clays was selected (Fig. 3).

### 3 Introduction of the semi-analysis solution method and numerical model

#### 3.1 Brief introduction of the semi-analysis solution method

The widely adopted governing equations of Biot (1956a, 1956b) are used to describe the motion of embankments and ground under moving train loads. Given that the track geometry and properties of high-speed railways remain consistent longitudinally, the dynamic response of both track and ground under moving train loads can be analyzed in the wavenumber domain. This approach enables the use of a 2.5D FEM to compute responses across the entire 3D space by evaluating responses in a 2D section for various wavenumbers. Detailed derivation procedures have been extensively documented (Gao et al., 2012; Bian et al., 2019).

Regarding changes in the water table, the region above it is treated as a single-phase medium. Fig. 4 describes the two-phase saturated medium and single-phase medium in the 2.5D FE model, where  $U_i$  and  $W_i$  ( $i=x, y, z$ ) represent the soil skeleton displacement and pore water displacement relative to soil skeleton, respectively,  $k_x$  represents the wavenumber along the  $x$  direction,  $\alpha$  and  $M$  are the Biot constants,  $n$  is the porosity,  $\rho_f$  is the density of the pore fluid,  $m$  is the effective density, and  $k_p$  is the soil permeability coefficient. For single-phase media, setting the liquid phase parameters

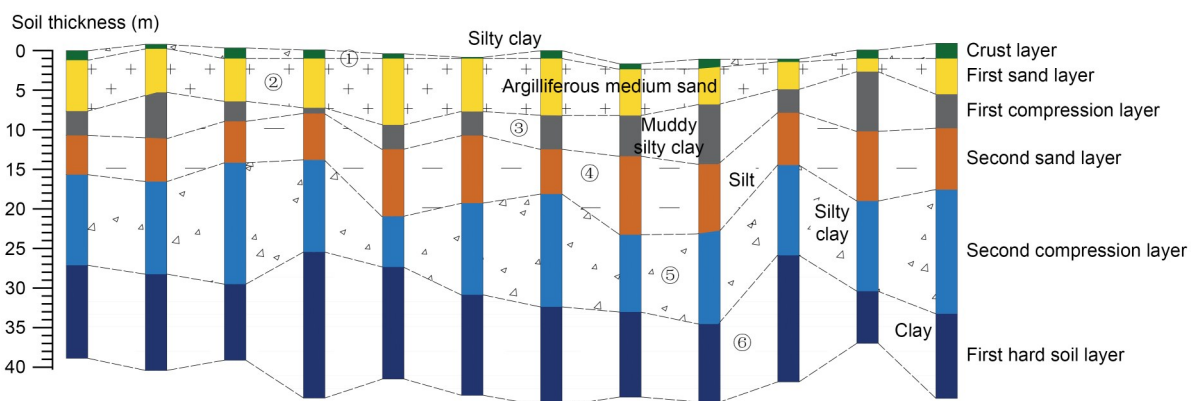
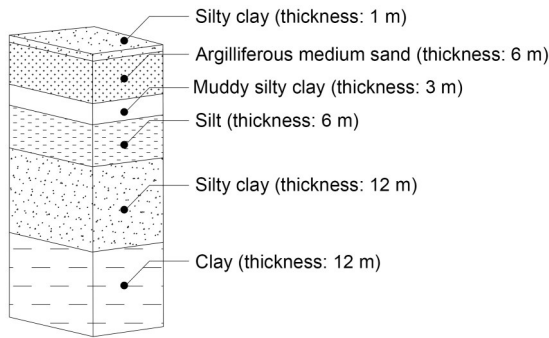
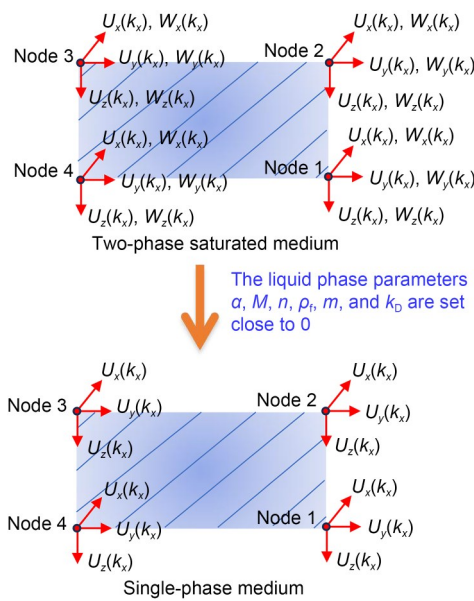


Fig. 2 Schematic view of a typical soil layer distribution of upper Shanghai clays



**Fig. 3** Simplified representation of foundation soil layers for upper Shanghai clays



**Fig. 4** Description of the two-phase saturated medium and single-phase medium in the 2.5D FE model

close to zero is sufficient (Hu et al., 2023). Subsequently, a 2.5D FEM saturated element can effectively model the behavior of single-phase media.

### 3.2 2.5D finite element model

Fig. 5 depicts the 2.5D FE model of the embankment and ground, where the total model depth is 42.7 m and the width is 100 m. Using symmetry, the model includes only 50 m. The embankment stands at a height of 2.7 m, including a 0.4 m roadbed layer and a 2.3 m subgrade layer. The soil layers in the foundation replicate upper Shanghai clays, detailed in Fig. 2. The embankment and soil layers are represented by 2.5D saturated linear elastic elements with 6 degrees of freedom per node. In the model, the embankment and foundation surfaces are free, while the left, right, and

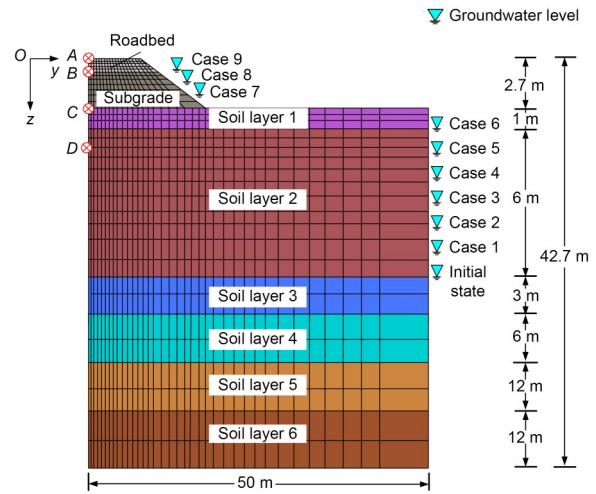


**Fig. 5** Schematic view of numerical model (not to scale)

bottom boundaries are fixed. To prevent wave reflection within the FE domain, a multi-layer damped boundary is implemented, as successfully demonstrated by Bian et al. (2019). The model includes three layers of damping on the left, right, and bottom sides, respectively. A nominal damping loss factor of 0.05 was assigned to the ground to avoid numerical issues. Moving outward from the inner part of the model, the damping values for each layer are 0.1, 0.2, and 0.4, respectively.

Four observation points, labeled *A* through *D*, are marked in Fig. 5. Point *A* is located at the surface of the embankment ( $z=0$  m), point *B* at the surface of the subgrade ( $z=0.4$  m), point *C* at the ground surface ( $z=2.7$  m), and point *D* at 1.7 m beneath the ground surface ( $z=4.4$  m). As indicated in Fig. 5, 10 different water tables were considered in this study. The water table was taken to rise gradually from the bottom of the sand layer, by 1 m between each case from the initial state to Case 6. Within the subgrade, three water levels were considered, with a rise of 0.8 m between them, up to the subgrade surface.

### 3.3 Model validation

Jiang et al. (2016a) constructed a full-scale model of a slab track–embankment system designed for Chinese high-speed railways. This physical model was used to assess the dynamic performance of the track–embankment system under various typical water tables. In this section, measurements of vibrations at the embankment surface were selected from the saturated foundation and saturated subgrade cases to validate the 2.5D FE model. Table 1 lists the parameters of the

**Table 1 Parameters of the full-scale physical model before/after a water table rise**

Layer number	Layer name	$\alpha$	$M$ (MPa)	Young's modulus, $E$ (MPa)	Poisson's ratio, $\nu$	$\rho_s$ (kg/m <sup>3</sup> )	$\rho_f$ (kg/m <sup>3</sup> )	Porosity, $n$	Permeability coefficient, $k_D$ (m/s)
Embankment	Roadbed	0.001	0.001	240	0.25	2200	0.001	0.001	$10^{-20}$
	Subgrade (before)	0.001	0.001	140	0.30	2000	0.001	0.001	$10^{-20}$
	Subgrade (after)	1	6400	80	0.30	2700	1000	0.30	$6 \times 10^{-4}$
Soil layers 1–6	Qiantang silty	1	3520	45	0.35	2700	1000	0.60	$1 \times 10^{-6}$

full-scale physical model before and after changes in the water table. Only the saturated foundation and saturated subgrade cases were simulated. The values in Table 1 are mostly referenced from Jiang et al. (2016b), where  $\rho_s$  is the density of soil particles.

As depicted in Fig. 6, the vibration velocities of the embankment surface calculated by the 2.5D FEM were compared with the results from model tests. The comparison shows that across train speeds ranging from 1 to 100 m/s, the results from the 2.5D FE calculations align closely with the test results. This validation underscores the accuracy of the 2.5D FE model.

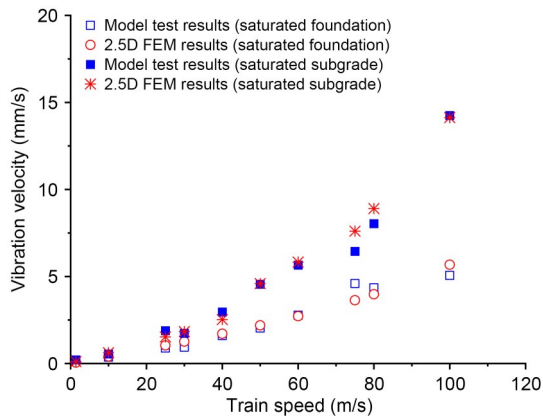


**Fig. 6 Verification of the 2.5D FEM via model test results**

### 3.4 Relevant properties for numerical analysis

According to geological investigations, most of the natural soil layers are normally in a high state of saturation; even the sand layer can have a saturation of about 70%. In the model, the embankment and foundation were therefore simulated by saturated media. Specifically, soil layer 2, the argilliferous medium sand layer, is represented in the initial state by a saturated element with a small permeability coefficient and a large modulus. As the water table rises, its permeability coefficient is increased, and its modulus is reduced (Mualem, 1976). In this way, a change of the water

table is introduced in this layer. Soil layer 1, the silty clay, is assumed not to change with the rise of the water table. For the embankment, its initial state is an approximate single-phase state, and thus the parameters  $\alpha$ ,  $M$ ,  $n$ ,  $\rho_b$ , and  $k_D$  were set close to 0, which means no water is contained in the embankment. The initial values of the soil materials for each layer are listed in Table 2. Since the water table changes only within the subgrade and argilliferous medium sand layer, the values for these two layers after water table rise are listed in Table 3. The parameters in both Table 2 and Table 3 are based on typical values from geological survey reports (Dassargues et al., 1991; Schroeder et al., 1992; Yan and Shi, 2006; Wu, 2016).

Table 4 shows the track parameters used in the simulation (Bian et al., 2019). The numerical simulation incorporated vehicle loads based on a six-car CRH2 train, using a quarter car model (Takemiya and Bian, 2005). The axle load is 144 kN. The specific parameters of the CRH2 are detailed in Table 5 (Bian et al., 2019).

## 4 Numerical analysis

### 4.1 Vibration responses

Fig. 7 illustrates the time-history curves of vibration displacement at point A on the embankment surface under different water tables, corresponding to train speeds of 30 and 70 m/s.

In Fig. 7a, it is evident that at a speed of 30 m/s, the shape of the dynamic displacement time-history curve at point A remains consistent across different water table conditions. As the water table rises from its initial state to Case 9, the maximum displacement at point A increases from 1.30 to 1.57 mm. The percentage increases in maximum displacement for each case are also shown in the figure. The rise in the water table within the subgrade notably affects the dynamic

**Table 2 Parameters for a typical Shanghai upper layer at initial state**

Layer number	Layer name	$\alpha$	$M$ (MPa)	Young's modulus, $E$ (MPa)	Poisson's ratio, $\nu$	$\rho_s$ (kg/m <sup>3</sup> )	$\rho_f$ (kg/m <sup>3</sup> )	Porosity, $n$	Permeability coefficient, $k_D$ (m/s)
Embankment	Roadbed	0.001	0.001	240	0.25	2200	0.001	0.001	$10^{-20}$
	Subgrade	0.001	0.001	140	0.28	2000	0.001	0.001	$10^{-20}$
Soil layer 1	Silty clay	1	3930	23	0.33	2730	1000	0.53	$2.9 \times 10^{-8}$
Soil layer 2	Argilliferous medium sand	1	6570	55	0.30	2600	1000	0.29	$1.6 \times 10^{-4}$
Soil layer 3	Muddy silty clay	1	3140	6.4	0.35	2600	1000	0.68	$2.0 \times 10^{-9}$
Soil layer 4	Silt	1	4540	36	0.34	2700	1000	0.45	$6.0 \times 10^{-6}$
Soil layer 5	Silt clay	1	4140	21	0.33	2730	1000	0.50	$8.9 \times 10^{-8}$
Soil layer 6	Clay	1	4540	38	0.33	2740	1000	0.45	$9.4 \times 10^{-9}$

**Table 3 Parameters after water table rise**

Soil layer	$\alpha$	$M$ (MPa)	Young's modulus, $E$ (MPa)	Poisson's ratio, $\nu$	$\rho_s$ (kg/m <sup>3</sup> )	$\rho_f$ (kg/m <sup>3</sup> )	Porosity, $n$	Permeability coefficient, $k_D$ (m/s)
Subgrade	1	6400	80	0.28	2000	1000	0.30	$6.0 \times 10^{-4}$
Argilliferous medium sand	1	6570	39	0.30	2730	1000	0.42	$2.4 \times 10^{-4}$

**Table 4 Parameters of slab track**

Parameter	Value
Rail mass per unit length (kg/m)	60.64
Rail bending stiffness (MN/m <sup>2</sup> )	6.625
Track slab bending stiffness (MN/m <sup>2</sup> )	40
Mass per unit length of track slab (kg/m)	950
Bending stiffness of concrete base (MN/m <sup>2</sup> )	190
Mass per unit length of concrete base (kg/m)	1800
Fastener stiffness (MN/m <sup>2</sup> )	28.5
Fastener damping (Ns/m <sup>2</sup> )	$5 \times 10^4$

**Table 5 Parameters used for the CRH2 train**

Parameter	Value
Carriage mass (kg)	45000
Bogie mass (kg)	3600
Wheelset mass (kg)	1700
Carriage length (m)	24.8
Center-to-center distance of adjacent bogies (m)	14.9
Bogie length (m)	2.5

response of the embankment more than when the water table rise is confined to the underlying ground. At a train speed of 70 m/s (Fig. 7b), the percentage increases in dynamic displacement for each case are similar to, or slightly higher than, those observed at 30 m/s. It is clear that the increase in water table leads to a significant rise of up to 23.57% in dynamic displacement, regardless of whether the train operates at low or high speeds.

Fig. 8 shows the percentage increase in displacement as a function of depth for each case, under train speeds of 30 and 70 m/s. Fig. 8 reveals that the displacement amplitude consistently increases compared to the initial state, demonstrating an amplification effect throughout the cross-section of both the embankment and ground due to changes in the water table. The increase in displacement response from rising water tables also affects regions below the new water table, with the greatest amplification occurring near the water table, particularly noticeable from Case 1 to Case 6. The depth-wise distribution shows more variability from Case 7 to Case 9, influenced mainly by the interfaces between different layers near the altered water table. Comparing Figs. 8a and 8b, it is evident that the overall amplification effect intensifies with increasing train speed.

Fig. 9 illustrates the evolution of maximum displacement responses at point A ( $z=0$  m) and point C ( $z=2.7$  m) as a function of train speed. At point C, the maximum response in each case is consistently smaller than at the surface.

Fig. 9a shows that for a high-speed railway constructed on typical upper Shanghai clays, the critical speed of the entire embankment-ground system in its initial state is about 87.5 m/s (315 km/h), which corresponds to the speed with the largest displacement amplitude. There are minimal variations in speed between 80 and 90 m/s across different water table cases. With

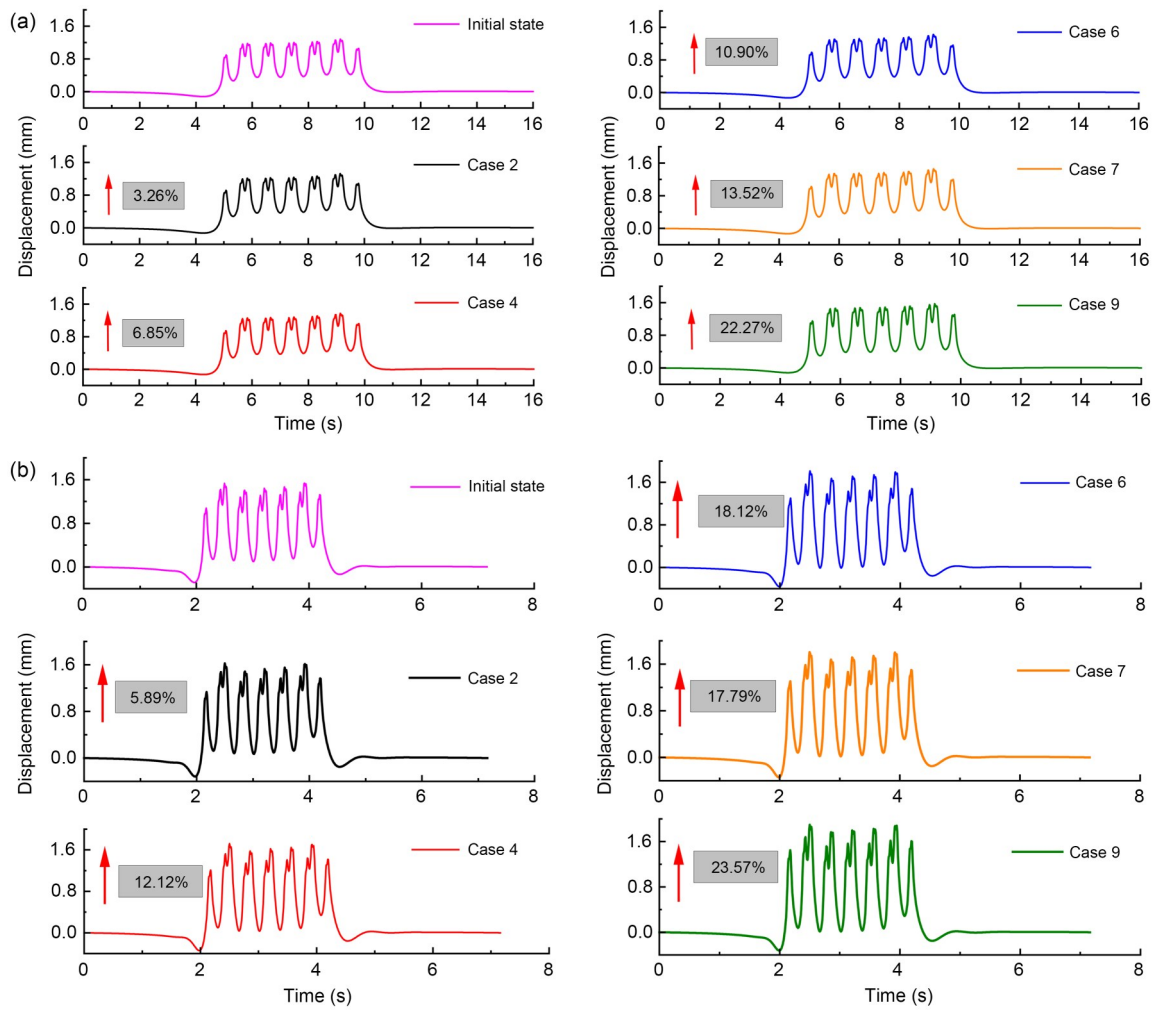


Fig. 7 Time-history curves of vibration displacement at point  $A$  ( $z=0$  m) under various cases and different train speeds: (a) 30 m/s; (b) 70 m/s

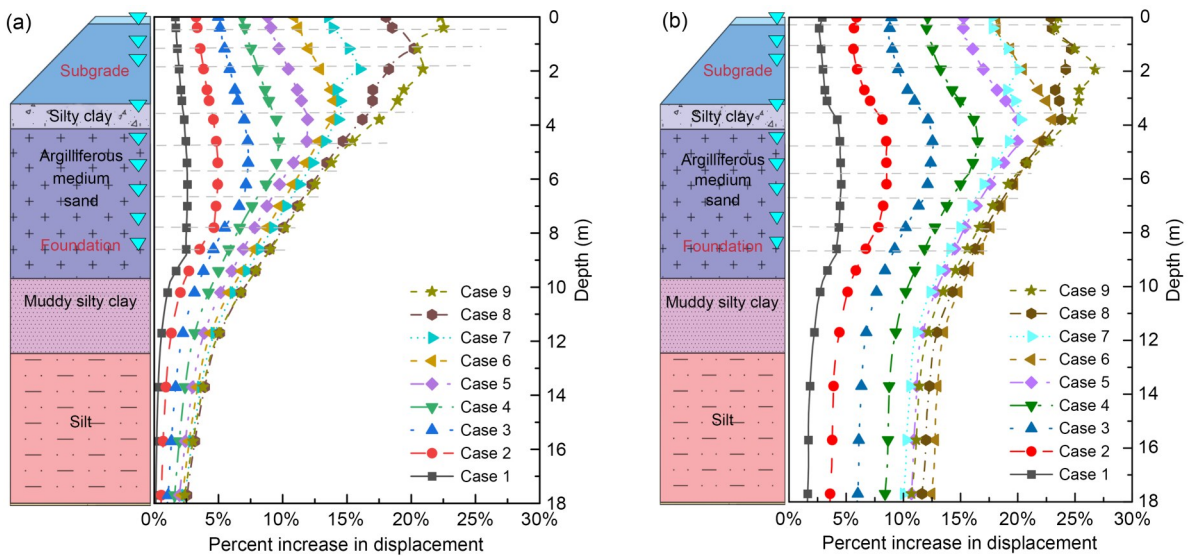


Fig. 8 Percentage increases in dynamic displacement for each case plotted against depth: (a) 30 m/s; (b) 70 m/s

an increase in water table, the critical speed of the system shows a slight variation, decreasing marginally to 85 m/s. A similar trend is observed in Fig. 9b regarding the maximum displacement responses of the foundation.

Considering the initial critical speed of around 90 m/s for the entire embankment–ground system, we conducted a frequency analysis of vibrations at a train speed of 90 m/s. Fig. 10 presents the frequency contents of vibration displacement at point A ( $z=0$  m) and point C ( $z=2.7$  m).

Fig. 10 depicts the frequency content data, highlighting peaks at about 3.6 and 10.8 Hz, along with their higher-order harmonic frequencies, observed at a train speed of 90 m/s. These dominant frequencies correspond to the passage of train carriages and individual bogies at the ends of coupled carriages, as discussed by Priest et al. (2010) and Bian et al. (2014).

Importantly, these dominant frequencies remain consistent across different water tables for both the subgrade and ground foundation. However, the amplitude increases with the water table. These findings are consistent with the measurement results of Jiang et al. (2016a). Moreover, a notable increase in amplitude in the frequency domain is observed as the water table rises within the subgrade. Another observed phenomenon is that, as depth increases, the amplitude of the vibration response in the frequency domain decreases rapidly. Additionally, different water table levels show slight variations in the rate of amplitude reduction, with a 90% decrease for the initial state and an 87% decrease when the water table rises to the subgrade.

Fig. 11 presents the 1/3 octave band frequency analysis at a speed of 90 m/s, based on vibration data from the subgrade surface. The analysis shows peak vibration velocities from 3.2 to 4.0 Hz and 8.0 to

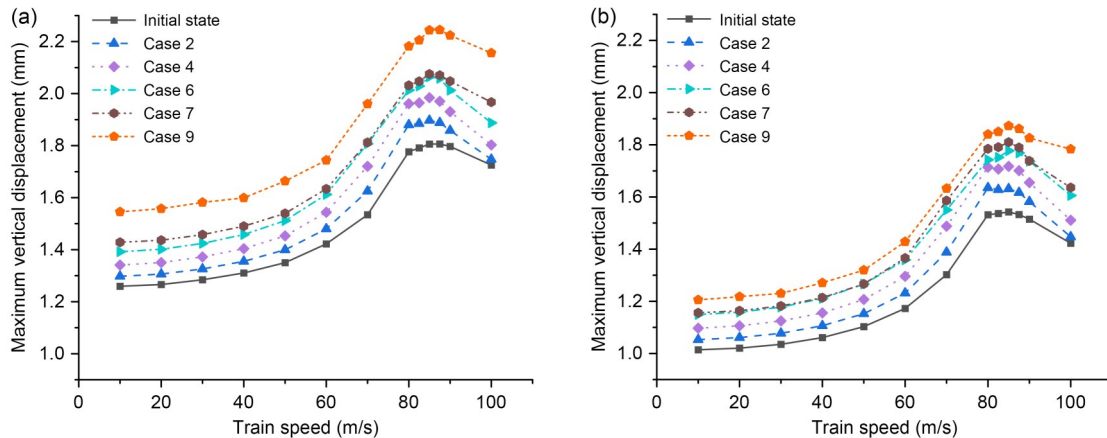


Fig. 9 Dependence of maximum displacement responses on train speeds for different depths and cases: (a) point A; (b) point C

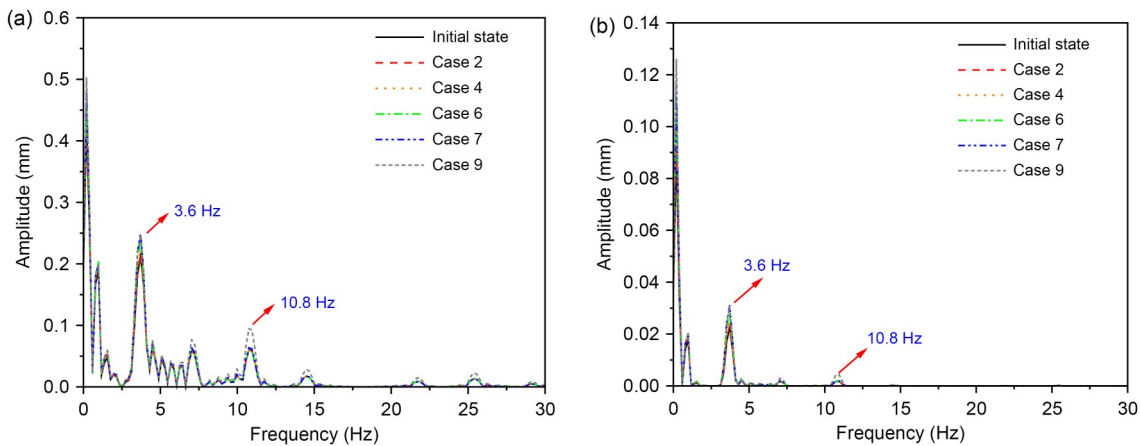


Fig. 10 Frequency spectrum analysis of the vibration displacement under a train speed of 90 m/s: (a) point A; (b) point C

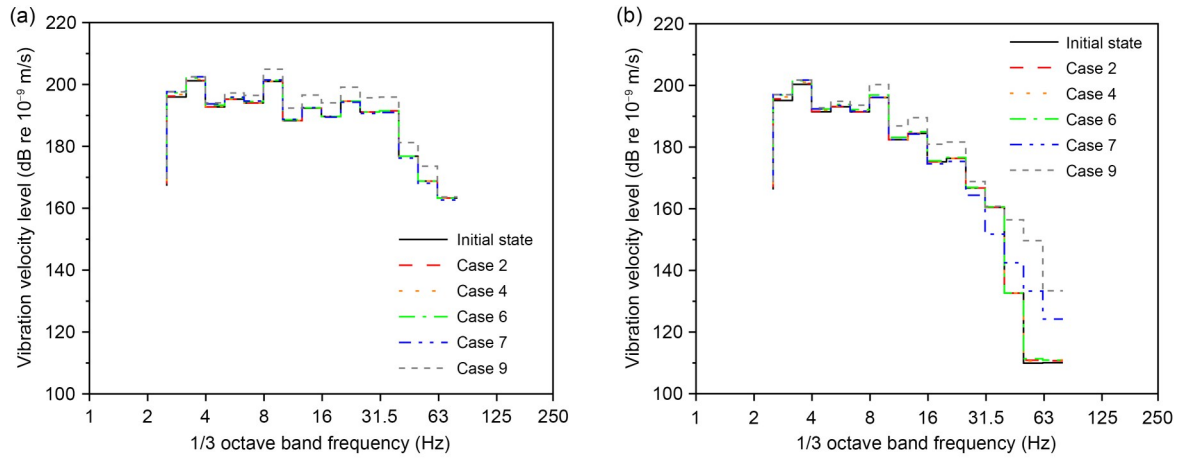


Fig. 11 The 1/3 octave band frequency analysis under a train speed of 90 m/s: (a) point A; (b) point C

10.0 Hz, attributed to the length of the train carriage and the adjoining bogies. Additionally, while there is a slight increase in vibration velocity as the water table rises in the ground, a significant increase is observed when the water table changes within the subgrade. The frequency range of peak vibration remains unchanged with increasing depth, but the intensification caused by a rising water table becomes increasingly evident. In the foundation, once the water table reaches the subgrade, the vibration amplitudes at high frequencies (greater than 31.5 Hz) in Cases 7 and 9 show quite significant increases.

#### 4.2 Excess pore pressure responses

Fig. 12 shows the vertical distribution of maximum excess pore pressure for different cases, including the initial state, for train speeds of 30 and 70 m/s. The maximum excess pore pressures exhibit a complex dependence on depth due to the variable permeabilities of the multi-layered foundation. For the initial state and Cases 1 to 6, the subgrade is treated as a single-phase medium, resulting in zero excess pore pressures. The silty clay layer has low soil permeability, leading to an increase in excess pore pressure. In contrast, the argilliferous medium sand layer has a much higher permeability, causing a decreasing trend in excess pore pressure within this layer. Near the bottom of the argilliferous medium sand layer, the presence of the muddy silty clay layer with lower permeability causes a slight increase in excess pore pressures with depth. Below the muddy silty clay layer, the excess pore pressure decreases to nearly zero due to the significant distance from the load.

Table 6 lists the peak values of excess pore pressure and their locations for each case at different train speeds. For the initial state at a train speed of 30 m/s, the peak excess pore pressure is 4.69 kPa, located in the silty clay layer at a depth of 3.6 m. As the water table rises in the argilliferous medium sand layer, its increased permeability results in a decrease in peak pore pressure values and a shallower depth at which the maximum value occurs. At a higher train speed of 70 m/s, this trend of decreasing peak values and their depths slows down. The deeper deformation depth caused by higher speed trains ensures that the peak excess pore pressure remains in the silty clay layer at a depth of 3.6 m, even in Case 7, when the water table rises to the subgrade. At higher train speeds, the peak excess pore pressure tends to appear deeper, with Case 9 showing a greater peak value. This could raise concerns about deformation in the deeper soft foundation soil. For both speeds, it is notable that in Case 9, with the water table rising significantly into the subgrade, substantial excess pore pressures are generated in the subgrade.

Fig. 13 illustrates the distribution of the maximum excess pore pressure responses in a cross-section of both the embankment and ground ( $y$ - $z$  plane) at a train speed of 70 m/s, about 0.8 times the embankment-ground system's critical speed, for the initial state and Case 9. To facilitate comparison of the size of the affected area in different cases, areas where the excess pore pressure exceeds 3 kPa are highlighted in red. The maximum values are indicated in the figures.

In Fig. 13a, the excess pore pressure is concentrated near the ground surface, peaking at about 4.84 kPa

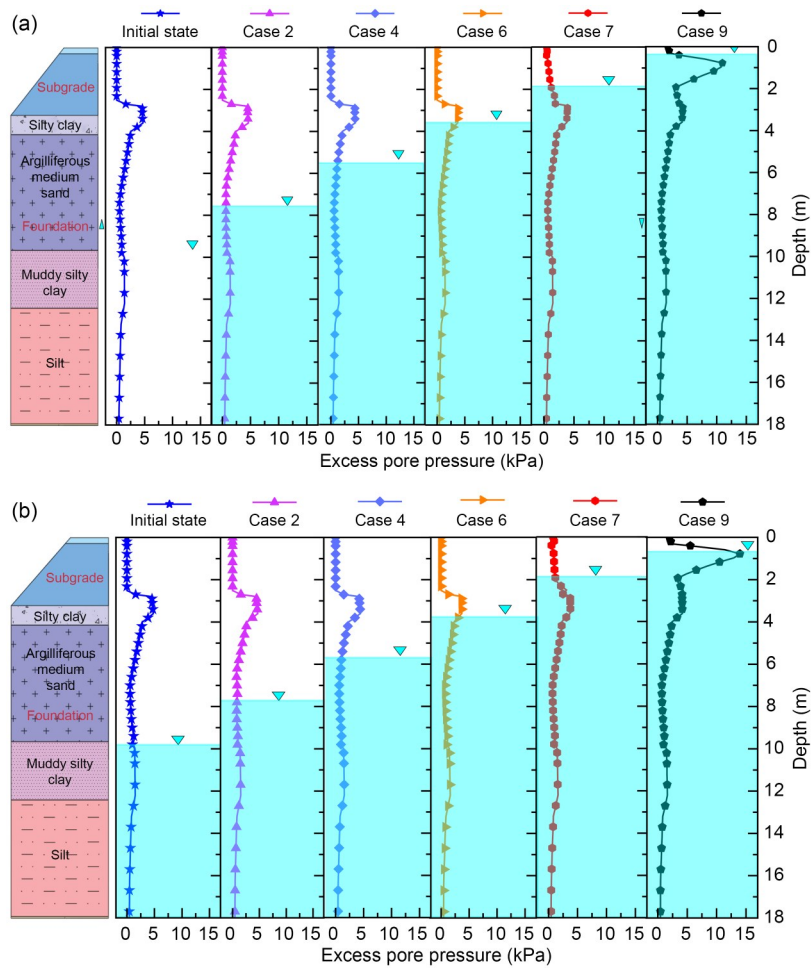


Fig. 12 Maximum excess pore pressures versus depth: (a) 30 m/s; (b) 70 m/s

Table 6 Peak excess pore pressures in different cases and their locations

Case	Train speed of 30 m/s		Train speed of 70 m/s	
	Peak excess pore pressure (kPa)	Location (m)	Peak excess pore pressure (kPa)	Location (m)
Initial state	4.69	3.6	4.79	3.6
Case 2	4.61	3.6	4.68	3.6
Case 4	4.41	3.6	4.46	3.6
Case 6	3.83	2.8	3.70	3.6
Case 7	3.98	2.8	3.77	3.6
Case 9	10.97	0.78	13.97	0.78

in the silty clay layer, with a parabolic distribution below this layer. Additionally, there is a region where the excess pore pressure exceeds 0.5 kPa at depths between 9 and 14 m. In Case 9, which features the highest water table, significant excess pore pressure extends across a considerable portion of the subgrade, forming an elliptical distribution. In this case, the maximum excess pore pressure is significantly higher, reaching about 23.21 kPa.

### 4.3 Effective stress analysis

Fig. 14 plots the stress paths at point *B*, the top of the subgrade, under two different cases and for train speeds of 30 and 70 m/s. The graph presents  $p$  ( $=(\sigma_1 - \sigma_3)/2$ ) against  $q$  ( $=(\sigma_1 + \sigma_3)/2$ ), where  $p$  is the mean principal stress,  $q$  is the mean deviating stress,  $\sigma_1$  is the maximum principal stress, and  $\sigma_3$  is the minimum principal stress. They are based on a coefficient of lateral

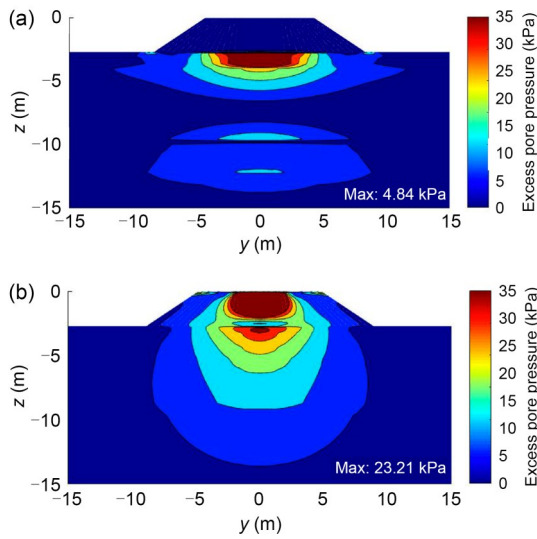


**Fig. 13** Excess pore pressure distribution contours of different cases in the  $y$ - $z$  plane at 70 m/s: (a) initial state; (b) Case 9. References to color refer to the online version of this figure

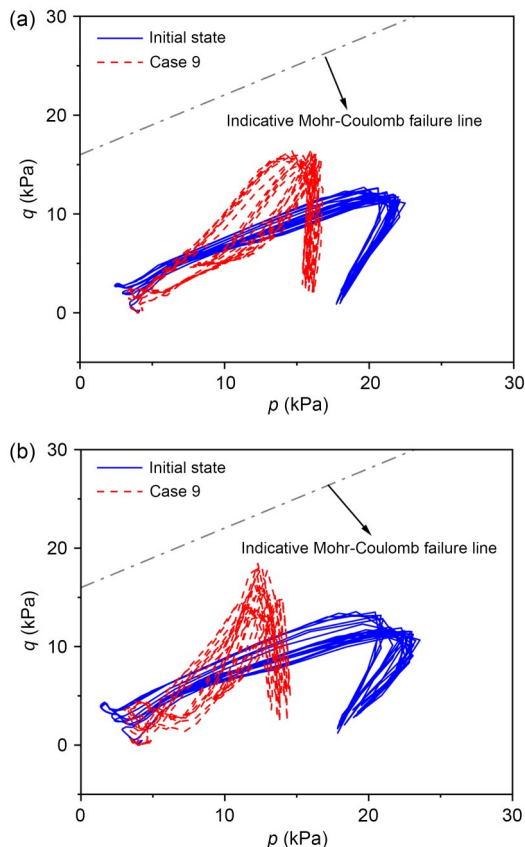


**Fig. 14** Effective stress path at point  $B$  under different train speeds: (a) 30 m/s; (b) 70 m/s

earth pressure  $K_0=0.5$ . According to Duong et al. (2013), the internal friction angle  $\varphi$  of the nearly saturated

embankment material is  $29^\circ$ , and its cohesion  $c$  is 21 kPa. An indicative Mohr-Coulomb failure line is also shown for reference. It is important to note that this failure line is included purely for illustrative purposes: since the analyses in this paper used purely elastic soil models, even if the stress path reaches the line, it does not imply soil failure.

Fig. 14 reveals that as the water table ascends to the surface of the subgrade, the stress path curve at point  $B$  shows a significant deflection towards the indicative Mohr-Coulomb failure line. This deviation becomes more pronounced with increasing train speed, bringing the stress path closer to the failure line. This suggests that both a rising water table and higher train speeds increase the likelihood of soil failure in the subgrade.

Fig. 15 shows the contour distribution of effective stress responses under a train speed of 70 m/s, for the initial state and Case 9. The effective stress reaction within the embankment is concentrated mainly in the impact zone of the train wheels and gradually diffuses as depth increases.

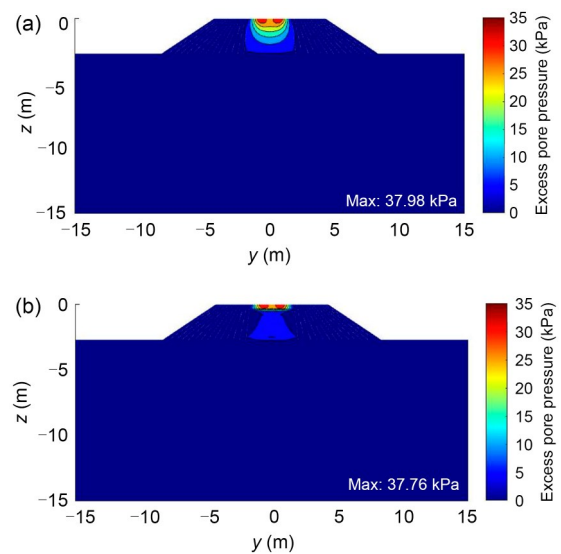


**Fig. 15** Contours of maximum effective stress for different cases in the  $y$ - $z$  plane at 70 m/s: (a) initial state; (b) Case 9

In the initial state, the effective stress response in the  $y$ - $z$  plane exhibits a smooth parabolic distribution, tapering down to 5 kPa at the base of the subgrade. For Case 9, with the highest water table, the effective stress response follows an approximately cylindrical distribution, diminishing to 5 kPa near the subgrade surface. A comparison of these two states reveals that

the rise in the water table within the subgrade leads to a rapid drop in effective stress with increasing depth, significantly increasing the susceptibility to subgrade instability.

## 5 Summary and conclusions

The increase in rainfall attributed to global warming has led to a rise in water table within subgrades and foundations, subsequently altering their dynamic behavior under train loads. Traditional analytical and numerical methods face significant challenges when addressing dynamic problems involving multi-layered saturated media and soil phase transformation. To address these challenges, in this study, we propose a 2.5D FE model that integrates both single-phase and saturated media. The model simulates the rise in water table by transitioning from a single-phase medium to a saturated medium. This study uses a representative soil layer from Shanghai to exemplify the foundation characteristics prevalent in the Yangtze River basin. The main findings of this study are as follows:

1. The rise in the water table amplifies the track's dynamic displacement. This increase in displacement amplitude is not confined to the depth of the water table change but affects the entire embankment–foundation cross-section. This amplification effect intensifies with higher train speeds.

2. For a high-speed railway built on typical upper Shanghai clays, the critical speed is around 85 m/s. While the rise in the water table significantly increases the displacement amplitude, it has minimal impact on the critical speed.

3. The vibration frequency of the embankment and foundation is influenced mainly by the length of the train carriage and the adjoining bogies. These dominant frequencies remain consistent across different water tables for both the subgrade and the ground foundation. However, the amplitude of these frequencies increases with the water table. Notably, there is a significant increase in amplitude when the water table rises within the subgrade.

4. Generally, the rise in the water table within the foundation decreases the peak values of excess pore pressure and the depth at which the maximum values occur. However, at higher train speeds, these decreasing trends slow down. The higher the train speed, the

deeper the position at which the peak excess pore pressure appears. When the water table rises within the subgrade, the peak values of excess pore pressure increase.

5. The rise in the water table within the subgrade has a more pronounced effect on the dynamic response of the embankment than on the ground foundation. When the water table rises into the subgrade, significant excess pore pressure is generated within the embankment. This condition brings the stress path closer to the indicative Mohr-Coulomb failure line, increasing the likelihood of soil failure in the subgrade.

6. The rise in the water table within the subgrade causes the effective stress to drop rapidly with increasing depth, reducing the soil's capacity and increasing the susceptibility to subgrade instability.

## Acknowledgments

This work is supported by the National Key Research and Development Program Young Scientist Project (No. 2024YFC2911000) and the National Natural Science Foundation of China (No. 52108308).

## Author contributions

Jing HU and Xuecheng BIAN designed the research. Jing HU and David THOMPSON processed the corresponding data. Jing HU wrote the first draft of the manuscript. Chengming YE and Juntao JIANG helped to organize the manuscript. Shujing WU revised and edited the final version.

## Conflict of interest

Jing HU, Chengming YE, Juntao JIANG, Shujing WU, David THOMPSON, and Xuecheng BIAN declare that they have no conflict of interest.

## References

- Ai ZY, Ji WT, Li Y, et al., 2021. Dynamic response of saturated multilayered soils with elastic superstrata subjected to vertical impulsive loadings. *Applied Mathematical Modelling*, 91:875-891. <https://doi.org/10.1016/j.apm.2020.09.019>
- Ba ZN, Liang JW, Jin W, 2015. Dynamic response of coupled system of track and layered fluid-saturated ground under moving high-speed loads. *Engineering Mechanics*, 32(11): 189-200 (in Chinese). <https://doi.org/10.6052/j.issn.1000-4750.2014.04.0323>
- Bai TH, 2014. New technologies applied in design and construction of Shanghai metro works. *Tunnel Construction*, 34(1):53-59 (in Chinese). <https://doi.org/10.3973/j.issn.1672-741X.2014.01.009>
- Bian XC, Jiang HG, Cheng C, et al., 2014. Full-scale model testing on a ballastless high-speed railway under simulated train moving loads. *Soil Dynamics and Earthquake Engineering*, 66:368-384.

- <https://doi.org/10.1016/j.soildyn.2014.08.003>
- Bian XC, Hu J, Thompson D, et al., 2019. Pore pressure generation in a poro-elastic soil under moving train loads. *Soil Dynamics and Earthquake Engineering*, 125:105711. <https://doi.org/10.1016/j.soildyn.2019.105711>
- Biot MA, 1956a. Theory of propagation of elastic waves in a fluid-saturated porous solid. I. Low-frequency range. *The Journal of the Acoustical Society of America*, 28(2):168-178. <https://doi.org/10.1121/1.1908239>
- Biot MA, 1956b. Theory of propagation of elastic waves in a fluid-saturated porous solid. II. Higher frequency range. *The Journal of the Acoustical Society of America*, 28(2):179-191. <https://doi.org/10.1121/1.1908241>
- Cai YQ, Sun HL, Xu CJ, 2008. Response of railway track system on poroelastic half-space soil medium subjected to a moving train load. *International Journal of Solids and Structures*, 45(18-19):5015-5034. <https://doi.org/10.1016/j.ijsolstr.2008.05.002>
- Chen RP, Zhao X, Jiang HG, et al., 2014. Model test on deformation characteristics of slab track-subgrade under changes of water level. *Journal of the China Railway Society*, 36(3):87-93 (in Chinese). <https://doi.org/10.3969/j.issn.1001-8360.2014.03.014>
- Costa PA, Colaço A, Calçada R, et al., 2015. Critical speed of railway tracks. Detailed and simplified approaches. *Transportation Geotechnics*, 2:30-46. <https://doi.org/10.1016/j.trgeo.2014.09.003>
- Dassargues A, Biver P, Monjoie A, 1991. Geotechnical properties of the Quaternary sediments in Shanghai. *Engineering Geology*, 31(1):71-90. [https://doi.org/10.1016/0013-7952\(91\)90058-S](https://doi.org/10.1016/0013-7952(91)90058-S)
- Duong TV, Tang AM, Cui YJ, et al., 2013. Effects of fines and water contents on the mechanical behavior of inter-layer soil in ancient railway sub-structure. *Soils and Foundations*, 53(6):868-878. <https://doi.org/10.1016/j.sandf.2013.10.006>
- Gao GY, Chen QS, He JF, et al., 2012. Investigation of ground vibration due to trains moving on saturated multi-layered ground by 2.5D finite element method. *Soil Dynamics and Earthquake Engineering*, 40:87-98. <https://doi.org/10.1016/j.soildyn.2011.12.003>
- Gao GY, Chen GQ, Li J, 2014. Numerical analysis of dynamic characteristic of transversely isotropic saturated soil foundation subjected to high-speed train load. *Chinese Journal of Rock Mechanics and Engineering*, 33(1):189-198 (in Chinese). <https://doi.org/10.13722/j.cnki.jrme.2014.01.014>
- Hu AF, Li YJ, Jia YS, et al., 2016. Dynamic response of a layered saturated ground subjected to a buried moving load. *Engineering Mechanics*, 33(12):44-51 (in Chinese). <https://doi.org/10.6052/j.issn.1000-4750.2015.04.0275>
- Hu J, Bian XC, 2022a. Analysis of dynamic stresses in ballasted railway track due to train passages at high speeds. *Journal of Zhejiang University-SCIENCE A (Applied Physics & Engineering)*, 23(6):443-457. <https://doi.org/10.1631/jzus.A2100305>
- Hu J, Bian XC, 2022b. Experimental and numerical studies on dynamic responses of tunnel and soils due to train traffic loads. *Tunnelling and Underground Space Technology*, 128:104628. <https://doi.org/10.1016/j.tust.2022.104628>
- Hu J, Bian XC, Xu WC, et al., 2019. Investigation into the critical speed of ballastless track. *Transportation Geotechnics*, 18:142-148. <https://doi.org/10.1016/j.trgeo.2018.12.004>
- Hu J, Tang Y, Zhang JK, et al., 2021. Dynamic responses of saturated soft soil foundation under high speed train. *Rock and Soil Mechanics*, 42(11):3169-3181 (in Chinese). <https://doi.org/10.16285/j.rsm.2021.0572>
- Hu J, Jin LL, Wu SJ, et al., 2023. Effect of groundwater level rise on the critical velocity of high-speed railway. *Water*, 15(21):3764. <https://doi.org/10.3390/w15213764>
- Huang CS, Zhou Y, Zhang SN, et al., 2021. Groundwater resources in the Yangtze River basin and its current development and utilization. *Geology in China*, 48(4):979-1000 (in Chinese). <https://doi.org/10.12029/gc20210401>
- Huang JJ, Su Q, Wang W, et al., 2019. Field investigation and full-scale model testing of mud pumping and its effect on the dynamic properties of the slab track-subgrade interface. *Proceedings of the Institution of Mechanical Engineers, Part F: Journal of Rail and Rapid Transit*, 233(8):802-816. <https://doi.org/10.1177/0954409718810262>
- Jiang HG, Bian XC, Jiang JQ, et al., 2016a. Dynamic performance of high-speed railway formation with the rise of water table. *Engineering Geology*, 206:18-32. <https://doi.org/10.1016/j.enggeo.2016.03.002>
- Jiang HG, Bian XC, Cheng C, et al., 2016b. Simulating train moving loads in physical model testing of railway infrastructure and its numerical calibration. *Acta Geotechnica*, 11(2):231-242. <https://doi.org/10.1007/s11440-014-0327-y>
- Lu JF, Hanyga A, 2005. Fundamental solution for a layered porous half space subject to a vertical point force or a point fluid source. *Computational Mechanics*, 35(5):376-391. <https://doi.org/10.1007/s00466-004-0626-5>
- Madshus C, Kaynia AM, 2000. High-speed railway lines on soft ground: dynamic behaviour at critical train speed. *Journal of Sound and Vibration*, 231(3):689-701. <https://doi.org/10.1006/jsvi.1999.2647>
- Mualem Y, 1976. A new model for predicting the hydraulic conductivity of unsaturated porous media. *Water Resources Research*, 12(3):513-522. <https://doi.org/10.1029/WR012i003p00513>
- Ng CWW, Li Q, Liu GB, 2011. Characteristics of one-dimensional compressibility of Shanghai clay. *Chinese Journal of Geotechnical Engineering*, 33(4):630-636 (in Chinese).
- Priest JA, Powrie W, Yang L, et al., 2010. Measurements of transient ground movements below a ballasted railway line. *Géotechnique*, 60(9):667-677. <https://doi.org/10.1680/geot.7.00172>
- Schroeder C, Dassargues A, Li XL, 1992. Engineering geological conditions in the central area of Shanghai. *Bulletin of the*

- International Association of Engineering Geology*, 46(1): 37-43.  
<https://doi.org/10.1007/BF02595031>
- Shen SL, Wu HN, Cui YJ, et al., 2014. Long-term settlement behaviour of metro tunnels in the soft deposits of Shanghai. *Tunnelling and Underground Space Technology*, 40: 309-323.  
<https://doi.org/10.1016/j.tust.2013.10.013>
- Takemiya H, Bian XC, 2005. Substructure simulation of inhomogeneous track and layered ground dynamic interaction under train passage. *Journal of Engineering Mechanics*, 131(7):699-711.  
[https://doi.org/10.1061/\(asce\)0733-9399\(2005\)131:7\(699\)](https://doi.org/10.1061/(asce)0733-9399(2005)131:7(699))
- Wu CJ, 2016. Depositional Environment and Geotechnical Properties for the Upper Shanghai Clays. PhD Thesis, Shanghai Jiao Tong University, Shanghai, China (in Chinese).  
<https://doi.org/10.27307/d.cnki.gsjtu.2016.001462>
- Xu B, Lu JF, Wang JH, et al., 2008. Dynamic response of layered saturated soil under moving loads. *Rock and Soil Mechanics*, 29(12):3186-3192 (in Chinese).  
<https://doi.org/10.3969/j.issn.1000-7598.2008.12.002>
- Yan XX, Shi YJ, 2006. Structure characteristic of engineering geology in Shanghai. *Shanghai Geology*, (4):19-24 (in Chinese).  
<https://doi.org/10.3969/j.issn.2095-1329.2006.04.005>
- Yuan ZH, Cai YQ, Cao ZG, 2016. An analytical model for vibration prediction of a tunnel embedded in a saturated full-space to a harmonic point load. *Soil Dynamics and Earthquake Engineering*, 86:25-40.  
<https://doi.org/10.1016/j.soildyn.2016.04.004>
- Zhou SH, He C, Di HG, 2016. Dynamic 2.5-D Green's function for a poroelastic half-space. *Engineering Analysis with Boundary Elements*, 67:96-107.  
<https://doi.org/10.1016/j.enganabound.2016.03.011>